submitted to *Geophys. J. Int.*

Characterizing the cover across South Australia: A simple passive-seismic method for estimating sedimentary thickness

Shubham Agrawal[1], Caroline M. Eakin[1], John O'Donnell [1,2]

[1]*Research School of Earth Sciences, Australian National University, Canberra, Australia*

[2]*Geological Survey of South Australia, Department for Energy and Mining, Adelaide, Australia.*

E-Mail: shubham.agrawal@anu.edu.au

10 July 2022

SUMMARY

A blanket of sedimentary and regolith material covers approximately three-quarters of the Australian continent, obscuring the crustal geology below and potential mineral resources within. Sedimentary basins also trap seismic energy increasing seismic hazard and generating noisy seismograms that make determining deeper crustal and lithospheric structure more challenging. The most fundamental question that can first be asked in addressing these challenges is how thick are the sediments? Borehole drilling and active seismic experiments using a controlled seismic source (e.g. vibroseis) provide excellent constraints, but they are limited in geographical coverage due to their expense, especially when operating in remote areas. On the other hand, passive-seismic experiments that involve the deployment of seismic receivers only (i.e. seismometers) are relatively low-cost and portable, providing a practical alternative for initial surveys. Here we utilize receiver functions obtained for both temporary and permanent seismic stations in South Australia, covering regions with a diverse sediment distribution. We present a straightforward method to determine the basement depth based on the arrival time of the P-converted-to-S phase generated at the boundary between the crustal basement and sedimentary strata above. Utilizing the available borehole data, we establish a simple predictive relationship between Ps arrival time and the basement depth, which could then be applied

to other sedimentary basins with some consideration. The method is found to work best for Phanerozoic sediments and offers a way to determine the sediment-basement interface in unexplored areas requiring only temporary seismic stations deployed for < 6 months.

Key words: South Australia – Receiver functions – Basement depth, Sediment thickness – Calibration

1 INTRODUCTION

The Australian continent is the flattest and one of the most tectonically stable continents on Earth, with the last major mountain-building event occurring $\sim$250 Ma (Pain et al., 2012). As a result, around $\sim$80% of the surface of Australia is masked by sediments, predominately Phanerozoic in age, obscuring the underlying crystalline basement. Onshore sedimentary basins in Australia vary in thickness, ranging from a few hundred meters to up to 15,000 m thick in the Fitzroy Trough within the Canning Basin, northwest Australia (Yeates et al., 1984). Many of these basins are rich in natural resources, such as base metals (and their subsidiaries), hydrocarbons, and groundwater (e.g. Hitzman et al., 2010; Leach et al., 2010). For instance, significant oil and gas reserves are being explored in the Cooper and Eromanga Basins of central Australia. Recent studies focusing on Australia have suggested that 15% of Australia is a prospective target for sedimentary rock hosted deposits (Hoggard et al., 2020). The abundance of Archean and Proterozoic blocks in Australia provides a potentially fruitful avenue for future explorations as sedimentary rock hosted metal minerals systems are largely associated with Proterozoic basins (e.g. Leach et al., 2010; Hitzman et al., 2010). A known example would be the Carpentaria Zinc Belt within the North Australian Basin System which contains three of the ten largest zinc-lead deposits globally (e.g. Southgate et al., 2013).

Australia's economy is heavily supported by natural resources and mining activity; however the majority of the easily accessible near-surface resources have already been found and, to a large degree, exploited (Mudd, 2007; Mudd et al., 2019). As such, the UNCOVER Initiative has become a national priority (Collett & McFadden, 2014), with the aim to improve the discovery potential

of new mineral deposits currently hidden beneath cover and thus keep pace with increasing global demand (Ali et al., 2017). Constraining the sedimentary rock thickness (i.e., depth of cover) is a fundamental component within this UNCOVER Initiative, under the core theme of "characterizing Australia's cover". Furthermore, sediment thickness estimates of basins with strong impedance contrast are of particular importance for seismic-hazard assessment. Amplification of the earthquake duration and shaking by energy trapped in sedimentary basins poses a significant risk to urban infrastructures around the world in heavily populated regions such as the Indo Gangetic Plains, the Atlantic Coastal Plain, the Los Angeles Basins, and the Kanto Basin (e.g. Srinivas et al., 2013; Liu et al., 2018; Cunningham & Lekic, 2020). While the seismic hazard in Australia is relatively low compared to tectonically active regions, some capital cities such as Sydney and Perth are co-located in basins and in regions of elevated hazard relative to the rest of Australia (e.g. 10% probability over 50 years of peak ground acceleration values ≥ 0.02g; Allen et al., 2020). For a better understanding and prediction of strong ground motions in populated sedimented regions, knowledge of sediment thickness is imperative. In addition, for tectonically active regions, basement depth (or basin structure) is also crucial in understanding the depth extent of faults, their geometry, offsets etc, which are useful for geoengineering and seismic hazard analyses.

The most accurate estimates of sedimentary rock thickness come from borehole drilling followed by active source seismic reflection/refraction imaging conducted using seismic vibrators or similar artificial seismic sources. While both provide excellent constraints, they are expensive (especially for deep boreholes) and require heavy machinery, such as a drill rig or vibroseis trucks, which can be logistically difficult to dispatch to remote locations with no sealed road network. As an alternative, passive-source seismology is non-invasive, relatively low-cost, and the only equipment required are the seismic receivers (for example, broadband or short period seismometers, seismic nodes etc.) that can be transported by off-road 4x4 vehicle or helicopter to remote locations that are not on the maintained road network (e.g. Rawlinson et al., 2017). Several passive-source seismic techniques currently exist to study the near-surface structure, such as the horizontal to vertical spectral ratio (commonly referred to as HVSR), spatial autocorrelation coefficient method,

receiver functions, and using the ambient seismic wavefield (e.g. Nakamura, 1989; Okada, 2006; Zheng et al., 2005).

Here we demonstrate the feasibility of using passive recording by single-station seismometers to infer the depth to crystalline basement directly. Utilizing a recent expanse in passive seismic deployments across South Australia (Fig. S1), and a wealth of existing drilling data in regions of exploration, we demonstrate a correlation between the depth to basement and the arrival time of the associated P-to-S converted phase. This relationship is calibrated from the existing borehole data and applied to predict the sedimentary rock thickness in under-explored remote regions where recent seismic deployments have occurred. While receiver functions have often been deployed previously to characterise the thickness of sedimentary basins, such studies typically required simultaneous determination of the associated velocity structure (e.g. Zheng et al., 2005; Srinivas et al., 2013; Yeck et al., 2013; Yu et al., 2015; Piana Agostinetti et al., 2018; Cunningham & Lekic, 2020; Wang et al., 2021). By calibrating an empirical relationship, we circumvent the need to determine any seismic velocities, and instead present a pathway for future studies to directly estimate the sedimentary thickness purely based on the observed arrival time. The method we employ is simple and straightforward to use, typically requiring only a few months of recorded data and is dependent only on the thickness of the sedimentary rock and the difference in average slowness between the P-wave and S-wave.It is however important to note that these empirical relationships have only been derived for South Australia so far, which has been tectonically stable since the Late Neoproterozoic. Such an approach will therefore most likely benefit other geologically similar areas with limited lateral heterogeneity relative to the scale of the study and regions that lack prior information about the sub-surface seismic velocities.

1.1 Sediment distribution and lithology of South Australia

South Australia has a rich geological history that stretches as far back as the Archean, with the origin of the Gawler Craton, the largest crustal province in South Australia (Hand et al., 2007). Within the craton lies Olympic Dam, the world's largest uranium resource, with significant copper

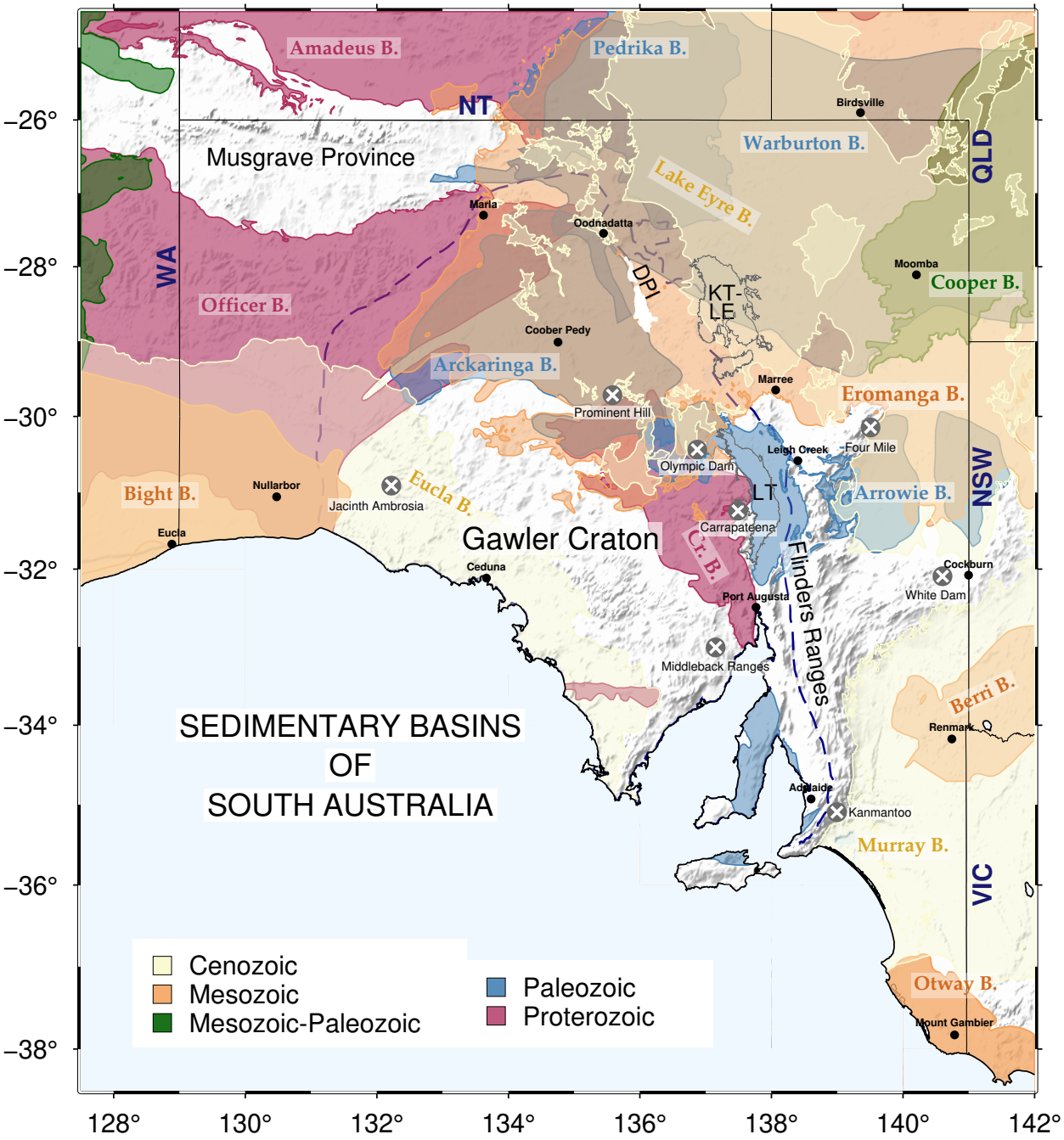

Figure 1. A comprehensive on-shore sedimentary basin map of South Australia. Basin information is acquired from the Geoscience Australia database (Raymond et al., 2018). Gray circles with white crosses are major approved/operating mines (see Data Availability section). The dashed blue line is the inferred boundary of the Gawler Craton. Abbreviations are as follows - Cr.B: Cariewerloo Basin, DPI: Denison and Peake inliers, KT-LE: Kati Thanda-Lake Eyre, LT: Lake Torrens, WA: Western Australia, NT: Northern Territory, QLD: Queensland, NSW: New South Wales, VIC: Victoria.

and gold reserves as well (e.g. Reid, 2019). Much of the mineral rich Gawler Craton, and indeed South Australia in general, is obscured by overlying sediments, with around a dozen or more major sedimentary basins across the state (Figs 1 and 2). The thickness of the sedimentary rock within these basins varies from 0 to $>$ 3,700 m, owing to a lengthy history of spatially varying sedimentation (Table 1).

Table 1. Summary of the onshore sedimentary basins of South Australia. Maximum sedimentary rock thickness and lithology information is acquired from the Geoscience Australia portal (https://portal.ga.gov.au/) and listed references. Density estimates are typically derived from active seismic lines or drillhole stratigraphic data. For each basin, the † symbol in Vp and density columns is indicative of that value being taken from the corresponding reference. Where not present, Vp and density values were inferred using the relevant relationships from Brocher (2005). Basins with * have significant off-shore sedimentation, however, the table lists on-shore properties of the sediments.

Basin	Period of deposition	Max. sedi. thickness	Lithology	Density (g/cc)	Vp (km/s)	Reference
Cariewerloo	Mesoproterozoic	1500m	Sandstone (metasediments)	2.65-2.75†	5.8-5.9†	Fraser et al. (2010)
Officer	Neoproterozoic to Devonian	3000m	Clastic & carbonates	2.55-2.75†	5.1-5.9	Baines et al. (2010)
Warburton	Cambrian to Devonian	1800m	Volcanic & sedimentary	2.3-2.6†	3.6-5.3	Baines et al. (2010)
Arrowie	Early to Mid Cambrian	4500m	Clastics, carbonates, redbed sandstones	2-2.4†	2.1-4.2†	Zang et al. (2004)
Pedrika	Permo-Carboniferous	1500m	Sandstones & oil-rich shales	2.1-2.4†	2.5-4.2†	Bishop (2012)
Arckaringa	Late Carboniferous to Permian	1000m	Siltstone, sandstone, shale	2-2.4†	2.1-4.2	Baines et al. (2010)
Cooper	Late Carboniferous-Middle Triassic	2500m	Sandstones & shales	2-2.3†	2.1-3.6	Radke (2009)
Eromanga	Early Jurassic – Late Cretaceous	2000m	Sandstone, siltstone, shale	1.9-2.4†	1.8-3.8†	Bishop (2012)
Bight*	Early to Late Cretaceous	350m	Sandstones & shales	1.8-2.4†	1.5-4.2	Barham et al. (2018)
Otway*	Late Jurassic-Cenozoic	7000m	Siliciclastic & volcaniclastic	1.8-2.4†	1.5-4.2	Brown & Stephenson (1991)
Berri	Cambrian-Ordovician	600m	Sandstone, mudstone, siltstone	-	-	Brown & Stephenson (1991)
Murray	Cenozoic	600m	Clay & limestone	1.5-2.3†	1.8-3	Li et al. (2021); Baines et al. (2010)
Eucla*	Cenozoic	150m	Limestone	1.5-2†	1.7-2.1	Barham et al. (2018)
Lake Eyre	Cenozoic	400m	Clay, silt, sand	1.5-2†	1.7-2.1	Baines et al. (2010)

The density of South Australian basement, primarily composed of the Gawler Craton and Curnamona Province, is in the range 2.7-3 gm/cc, as modelled using gravity and active seismic data resulting in expected P-wave velocities of the crustal basement generally between 5.8-6.2 km/s (Korsch et al., 2010; Bishop, 2012; Fraser et al., 2010; Baines et al., 2010). The sedimentary history and the corresponding lithology of South Australian basins is summarised in Table 1. The basins can be categorized into five age groups, Proterozoic, Early Paleozoic, Late Paleozoic, Mesozoic, and Cenozoic. The oldest intra-cratonic Proterozoic basins Cariewerloo and Officer (pink regions in Fig. 1) have well compacted and partially metamorphosed sedimentary rocks yielding seismic velocities of $\geq$ 5 km/s and densities approaching similar values to the basement (column 5 of Table 1). There are two Early Paleozoic basins in South Australia, the Warburton and Arrowie Basins (blue regions Fig. 1), with deposition stretching as far back as the Cambrian period. The Arrowie Basin is thicker and deeper with sedimentary thicknesses in excess of 3000m in its centre, although the spatial extent is more limited (Zang et al., 2004). The Warburton Basin has a higher range of expected velocities (Vp $\sim$ 3.6-5.3 km/s) due to a combination of volcanic and sedimentary deposits (Table 1; Bishop, 2012). In comparison, the Arrowie Basin is composed of a mixture of clastic, carbonate, and sandstone rock resulting in lower average densities and P-wave velocities in the range 2.1-4.2 km/s (Zang et al., 2004). There are two additional Late Paleozoic basins, the Pedricka and Arckaringa Basins dating back to the Carboniferous-Permian period. Both have maximum sedimentary thicknesses of 1000m or more and similar compositions (sandstone and shales) resulting in similar expected velocities of 2.1-4.2 km/s for Vp (Table 1; Korsch et al., 2010; Bishop, 2012). The Cooper Basin in the northeast corner of the state (green Fig. 1) straddles the Late Paleozoic to Early Mesozoic, with sandstone and shales deposits of considerable thickness (up to 2500m) and similar seismic velocities to the Late Paleozoic basins. The Cooper Basin is particularly famous for its prolific oil and gas reserves located $\sim$ 1250m below the surface, and has been relatively well explored (Radke, 2009).

The Mid-to-Late Mesozoic (orange Fig. 1) saw substantial sedimentation occur across South Australia with the Eromanga, Bight, Otway, and Berri Basins all forming during this time. The Ero-

manga Basin in particular is spatially extensive covering the older Cooper and Warburton Basins below (Fig. 1), and playing host to the aquifer system the Great Artesian Basin (Drexel & Preiss, 1995). The Mesozoic basins have generally similar sedimentary lithologies (e.g. sandstones), but with maximum thicknesses varying from several hundred to several thousand metres (see Table 1) and with a wider range of expected velocities (Vp $\sim$1.5-4.2 km/s). The Bight and Otway Basins are notable for significant offshore deposits and have been identified for potential exploration (e.g. Barham et al., 2018). Most recently, during the Cenozoic (yellow Fig. 1), three large-scale sedimentation episodes occurred, including the Eucla, Murray and Lake Eyre Basins (Barham et al., 2018; Brown & Stephenson, 1991). These are mostly thinner/shallower ($\leq$600m) deposits with sedimentary lithologies of clays and limestone that differ slightly from older basins (Table 1). The expected seismic velocities in these Cenozoic basins are less than 3 km/s, suggesting the presence of unconsolidated sediments.

Given the abundance of sedimentary basins and associated sub-surface natural resources in South Australia, there have been more than 27,100 onshore boreholes drilled (see Data Availability section) that determined the depth to basement (Fig. 2). The basement depth values range up to 3700 m, with the deepest values in the Cooper-Eromanga Basin area around Moomba. The vast majority ($\sim$94%) of boreholes have been drilled in places with sedimentary rock thickness less than 200 m (Fig. S2). The highest concentration of deeper boreholes ($>$ 1400 m) is within the Cooper-Eromanga Basin, with more than 900 boreholes drilled to the basement.

2 DATA AND METHODS

2.1 Receiver functions in sediments

Receiver functions (RFs) are an effective and commonly used tool to image seismic discontinuities within the Earth's crust and mantle arising from changes in the material properties. The RF technique focuses on converted phases - typically P to S conversions (Ps) in the P-wave coda - arising from seismic velocity discontinuities below the receiver (i.e. a seismic station)(Vinnik, 1977; Langston, 1979; Ammon, 1991). To remove the effect of source-side structure and wave-

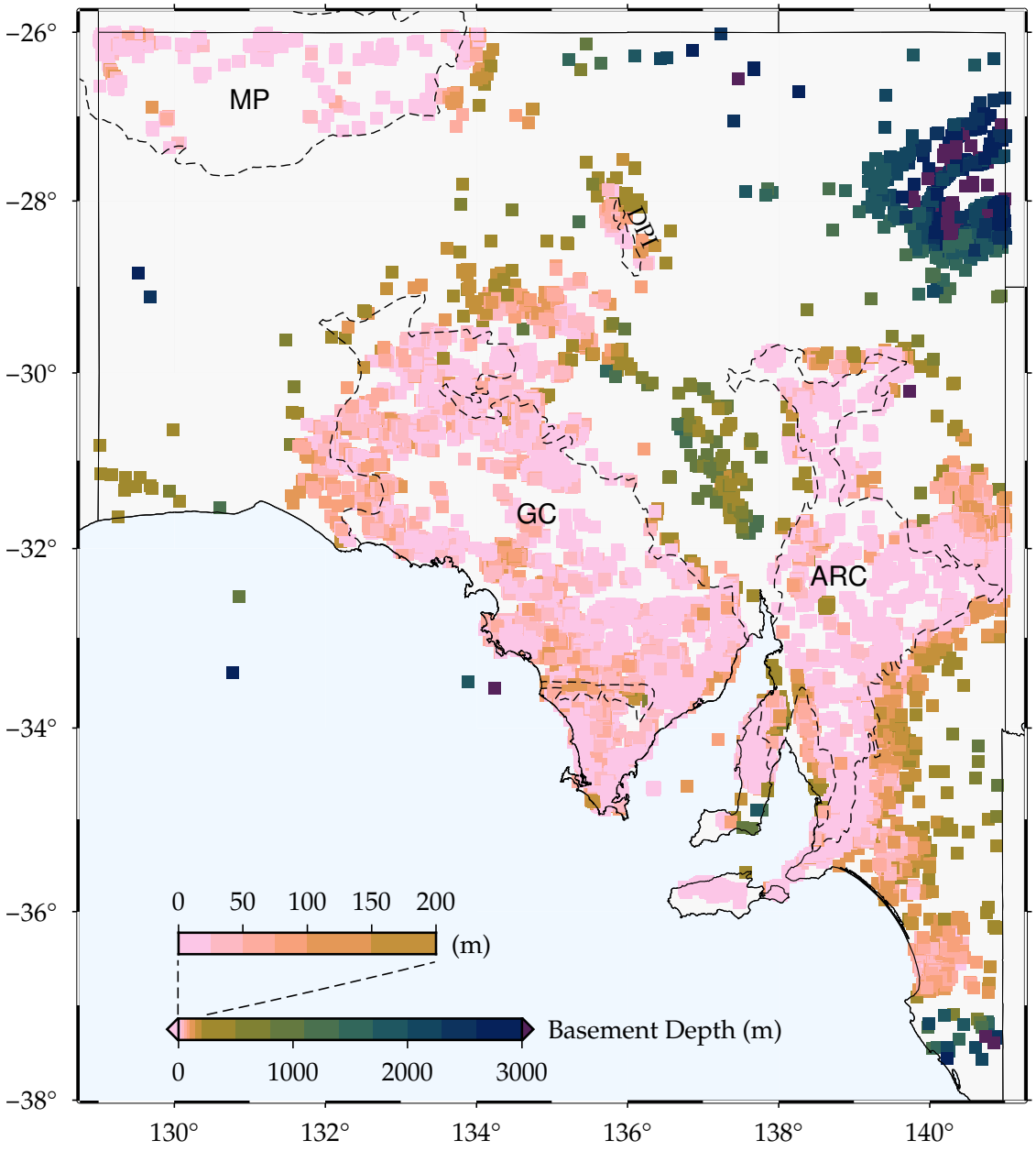

Figure 2. Individual borehole basement depth measurements (coloured squares) for the state of South Australia (see Data Availability section). The black dashed lines are geological provinces (MP: Musgrave Province; GC: Gawler Craton; ARC: Adelaide Rift Complex) with little or no sediment cover (Raymond et al., 2018). The colour scale is adjusted in the upper 200 m to encapsulate the variations in depth.

field propagation, the vertical component (dominated by P-wave energy) is deconvolved from the radial component seismogram (containing energy from both P and S waves) to obtain the radial RF, hereafter simply referred to as the RF (e.g. Ligorría & Ammon, 1999).

RFs have been employed extensively to image the Moho (crust-mantle boundary), the lithosphere-

asthenosphere boundary, and the 410 km and the 660 km global seismic discontinuities (e.g. Kennett et al., 2011; Birkey et al., 2021; Tauzin et al., 2013). However, only a few have used RFs to constrain the properties of the sedimentary layers without forward modeling (e.g. Zheng et al., 2005; Srinivas et al., 2013; Yeck et al., 2013; Yu et al., 2015; Piana Agostinetti et al., 2018; Cunningham & Lekic, 2020; Wang et al., 2021). In the presence of a sedimentary layer, RFs are dominated by strong reverberations after the arrival of the direct-P phase. These can last for several seconds and can mask the signal from deeper crustal discontinuities (e.g. Tao et al., 2014; Zelt & Ellis, 1999). This occurs due to the significant impedance contrast between the low-velocity sedimentary layer and the basement rock, trapping the P and S waves in the sediment layer. The predictability of the reverberations can be exploited however, through autocorrelation of the radial receiver function, to determine the two-way travel time of S-waves in the sedimentary layer (Yu et al., 2015). Using this information the seismic properties of the sedimentary strata can be directly determined, such as the fundamental frequency or the shear-wave velocity if the thickness is known (e.g. Cunningham & Lekic, 2020). Alternatively, using this information a resonance removal filter can be constructed to essentially reverse the sediment reverberation effect and thus aid the detection of later arrivals on the RF from deeper P-to-S conversions such as at the Moho or lithosphere-asthenosphere boundary (e.g. Cunningham & Lekic, 2020; Yu et al., 2015; Zhang & Olugboji, 2021).

The presence of a sedimentary layer can have some additional customary effects on the RF signal. When the incoming teleseismic P-wave enters the lower-velocity sedimentary rock, the angle of incidence steepens (due to Snell's Law), and the ray becomes nearly vertical (Fig. 3). The energy of the direct-P wave is, therefore mostly confined to the vertical component, with minimal energy on the horizontal components (radial and transverse). The amplitude of the first P-arrival on the radial RF, therefore, decreases as the incidence angle steepens and the pulse width is broadened (Cassidy, 1992; Sheehan et al., 1995; Zelt & Ellis, 1999). Instead, the P-to-S converted phase between the basement and sediments often becomes the first large amplitude signal on the radial RF, and can completely mask the low amplitude direct P-wave (Yeck et al., 2013; Yu et al.,

2015). We term this phase Ps_b and focus on its arrival time on the radial RF relative to the direct P-arrival on the vertical RF to estimate the depth to basement. An increase in the thickness of the sedimentary layer leads to a later arrival of the Ps_b phase (Zelt & Ellis, 1999). As the Ps_b phase is the first large amplitude arrival on the radial RF it is relatively easy to distinguish even in the presence of strong sediment reverberations and remains unaffected by such reverberations.

2.2 Seismic stations and receiver function computation

In the last several years, there has been an expansion in the number of passive seismic deployments across South Australia (Fig. S1). While coverage is still non-uniform and occasionally sparse, the addition of new networks in increasingly remote locations allows for the investigation of Earth's structure in under-explored regions within the continental interior that are typically less accessible to other methods. Most recently, the Marla Line (Liang & Kennett, 2020), Lake Eyre Basin (Eakin, 2019), and AusArray-SA (ODonnell et al., 2020) experiments have increased coverage over the eastern margin of the Gawler Craton, and the various sedimentary sequences that cover it. The Lake Eyre Basin seismic array, as the name suggests, has increased coverage surrounding Kati Thanda-Lake Eyre where the sediment cover is thickest within South Australia, and was the first experiment to install broadband and short-period seismometers across the remote Simpson Desert.

Overall data from twelve temporary and two permanent seismic networks (AU and S1), with stations located across South Australia, were used for analysis in this study (see Data Availability section; Fig. S1). In addition, some stations situated just beyond the state borders were included where available, such as the AQT network (1Q) in southwest Queensland. For the Marla Line experiment (3G), which had dense station spacing of < 4km, we selected only every 5^{th} station. Both short-period and broadband seismic stations (channels SH*, HH*, BH*, and EH*) were utilized for the receiver function analysis, comprising 243 individual seismic stations in total.

For each station, three-component data for earthquakes of Mw ≥ 5.5 and in the distance range of 30° - 95° was sought (Fig. S3 shows the availability of earthquakes for station AEB15, as an

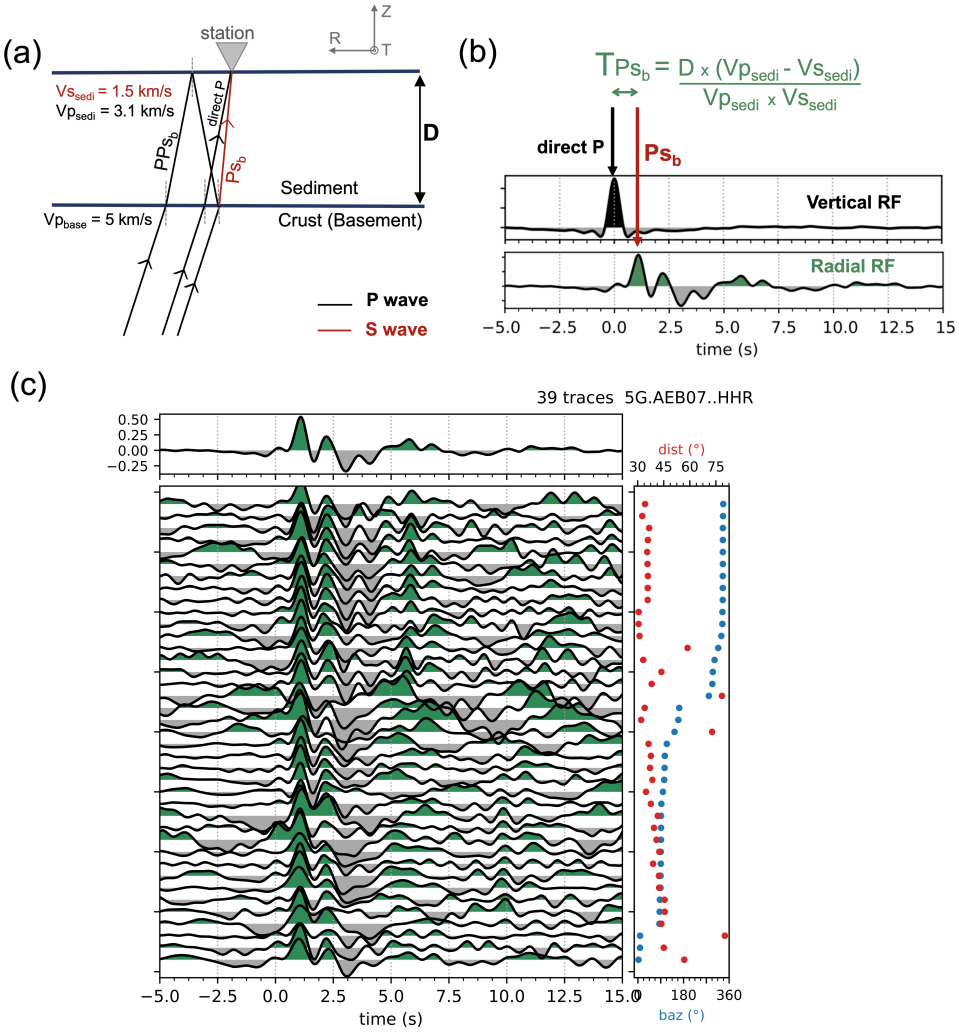

Figure 3. a) Schematic ray paths of P and S waves traversing a sediment layer (of thickness D) in response to an incoming P wave from an epicentral distance of 60° for the shown velocity structure. b) An example of TPs_b estimation from receiver functions at typical station AEB07. The station is located on thick sedimentary rock cover (see Fig. 5 for location), hence the significant delay in the Ps$_b$ phase relative to direct P. The formula for TPs_b is derived assuming vertical incidence of P and S waves beneath the station. c) Individual receiver functions that passed the quality control for station AEB07, which were used to calculate the stacked receiver function. The right panel provides epicentral distance (red dots) and backazimuth (blue dots) values for each receiver function.

example station). For temporary networks, typically a minimum of four months recording provided more than 75 earthquakes; however, on average, more than 150 earthquakes were available for each station. For permanent stations, earthquakes were sought from the previous year (2020), as this provided sufficient RFs for the analysis. The extracted 200 s of seismograms around the ex-

pected (using iasp91; Kennett & Engdahl, 1991) teleseismic P-arrival (50 s before and 150 s after) were then demeaned, detrended (linear), cosine tapered, and bandpass filtered between 0.1-1 Hz. Only earthquakes with a signal-to-noise ratio $\geq$ 1.5 (noise window: 45 s to 15 s prior to predicted P; signal window: 5 s before to 25 s after predicted P) were kept. The radial RFs were computed (using the iasp91 predicted P-arrivals) through the rf Python-package (Eulenfeld, 2020), using an iterative time-domain deconvolution (Ligorría & Ammon, 1999). Each RF was then stretched and compressed on the time axis using a reference slowness of 6.4 s/° (moveout correction) since the arrival times of converted phases are influenced by the slowness of the ray as well. Further, to ascertain the quality of individual RFs and the subsequent stacks, only radial RFs where the largest arrival is a positive polarity peak within the first 2 s were kept. Stations with at least ten good RFs were then stacked (an example is shown in Fig. 3c). Out of 243 stations, 231 met this criterion and were used for further analysis. All 231 stacked RFs are presented in Fig. 4 and the corresponding list of measurements in Table S1.

Using the RF stack for each station, the Ps_b arrival time (i.e. the P-wave converted to S-wave at the basement-sediment boundary) was determined with respect to the direct P-wave arrival on the vertical receiver function, hereafter referred to as TPs_b. As illustrated in Fig. 3, in the presence of sediments, the direct P-wave has near-vertical incidence beneath the seismic station and thus has a small amplitude on the radial RF. Instead, the largest positive peak on the radial RF is the Ps_b phase, which arrives shortly after ($\sim$1 s for station AEB07) the direct P on the vertical RF. The relative time difference between the largest positive peak on the radial RF and the vertical RF is, therefore, simply measured for each station to estimate TPs_b, which is primarily a function of the sedimentary rock thickness (Fig. 3).

3 RESULTS AND DISCUSSION

3.1 TPs_b observations and frequency dependence

As previously noted, the effect of sediments on RFs has been well established (Cassidy, 1992; Sheehan et al., 1995; Zelt & Ellis, 1999), and many of these known traits can be observed in the

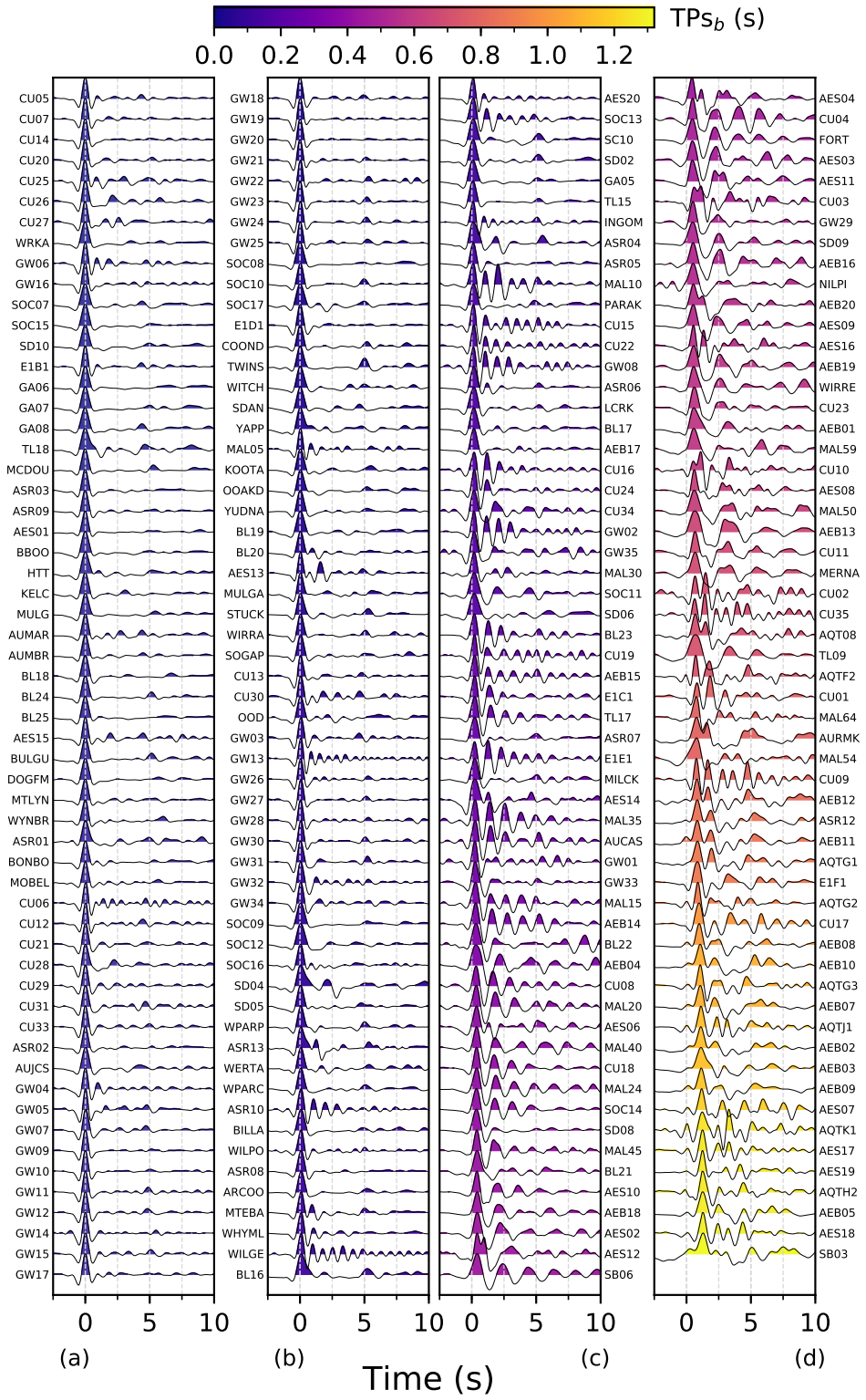

Figure 4. Stacked radial receiver functions for 231 seismic stations which had at least 10 individual receiver functions that passed the quality control. The stacks are coloured and sorted by the TPs_{b} value. Station name is printed next to the waveform.

radial RFs for South Australia (Fig. 4). We primarily focus our attention on the phase Ps_b and potential coeval phases. In Fig. 4, stations are arranged by increasing TPs_b values, from top left to bottom right, with each individual stacked RF coloured according to the TPs_b value. The first two columns show classic RFs with a relatively large dominant pulse centered on zero seconds (i.e. closely corresponding to the direct P-wave arrival time). In the third column, for TPs_b values of 0.1 to 0.5 seconds, characteristic sediment reverberations become unmistakable with a ringing signal continuing up to 10 sec or longer. This ringing behaviour is most evident is stations such as WILGE, GW08, MAL35, AEB14, SB06 etc. However, the time extent of the reverberations differ from station to station as it primarily depends on the impedance contrast between the sediment layer and the crystalline basement (Cassidy, 1992; Sheehan et al., 1995; Zelt & Ellis, 1999).

Further, as the TPs_b values increase, there is a systematic broadening, and positive offset from zero, of the first arrival pulse. This is an expected signature of RFs in the presence of increasing sedimentary thickness due to the overlapping arrival of reflected/refracted phases that interact with the sedimentary package, such as Ps_b, PPs_b, PSs_b etc. (the reader is directed to Cunningham & Lekic, 2020, 2019, for further details and extensive modeling of such phases). Since this study makes use of the first-arrival, the two prime prospects are Ps_b and PPs_b phases. For thin sediments ($TPs_b \leq 0.3$), there is very little difference in the arrival time of the two phases and thus a sharp single first pulse is observed (Fig. 4 a-b). For $0.3 \leq TPs_b \leq 0.6$, however, the time difference between the two phases is expected to grow but still overlap, resulting in the merging of Ps_b and PPs_b phases which are slightly offset from each other, and consequently the broadening of the first pulse.

It is possible to visually separate the Ps_b and PPs_b phases if higher frequencies are included in the RF calculation (Cunningham & Lekic, 2019). To consider the effect of this on our measurements, we analyse RFs for 38 stations from the Lake Eyre array using higher frequency cut-offs of 2.5 Hz and 4 Hz (Fig. S4). The Lake Eyre array was particularly well suited for this exercise as it spans the entire observed TPs_b range (0 - 1.3 sec). As seen in Fig. S4, the TPs_b difference between the different frequency bands is most prominent between 0.4 - 0.6 sec, with differences

of up to 0.125 seconds seen (with the exception of station AES14). For $TPs_{\mathrm{b}} \geq 0.6$ sec, the difference in TPs_{b} between different frequencies reduces to around zero as the two phases are largely separated and distinguishable in all frequency bands. Although including higher frequencies does help separate the $\mathrm{Ps_b}$ and $\mathrm{PPs_b}$ phases, we prefer the 0.1 - 1 Hz filter for the RF analysis for two reasons. Firstly, including the higher frequencies makes the RF noisier due to the inclusion of higher frequency noise, which reduces the overall $\mathrm{Ps_b}$ phase picking accuracy (i.e. lower signal-to-noise ratio). Secondly, the 0.1-1Hz frequency band doesn't always overestimate the first arrival, with differential TPs_{b} values that are both positive and negative, and thus higher frequency RF do not always give a consistent result that would suggest improved accuracy of $\mathrm{Ps_b}$ phase picking (Fig. S4). Depending on the particular objectives, lower frequency cut-offs may not always be better, but for this study we find that the chosen lower frequency band performs best for our automated procedure.

3.2 Spatial variation of TPs_{b}

The TPs_{b} values measured across 231 stations reveal striking geographical patterns (Fig. 5). The TPs_{b} values are highest in the northeast of the study area while lowest for stations on the southern Gawler Craton. The highest TPs_{b} value of 1.32 s was recorded at station SB03 (Skippy network; 7B) situated atop the Cooper and Eromanga Basins. The majority (61%) of stations registered $TPs_{\mathrm{b}} \leq 0.2$ s, while 16 stations ($\sim 7\%$) had $TPs_{\mathrm{b}} \geq 1$ s.

Areas of elevation and outcropping basement - such as the southern Gawler Craton, Flinders Ranges, and Musgrave Province - have TPs_{b} values close to zero, indicating minimal sedimentation in such regions (gray areas in Fig. 5). On a smaller scale, stations OOD, AEB17, SD06, and AES15 installed on top of the Denison and Peake Inliers (DPI in Fig. 2), a small basement outcrop to the west of Kati Thanda-Lake Eyre, display $TPs_{\mathrm{b}} \sim 0$ s, while surrounded by stations with $TPs_{\mathrm{b}} \geq 0.4$ s that lie beyond the basement inlier. Moderate values of TPs_{b} ($\sim$0.5 s) are co-located with regions with significant sediment accumulation, such as the Berri, Arrowie, Bight,

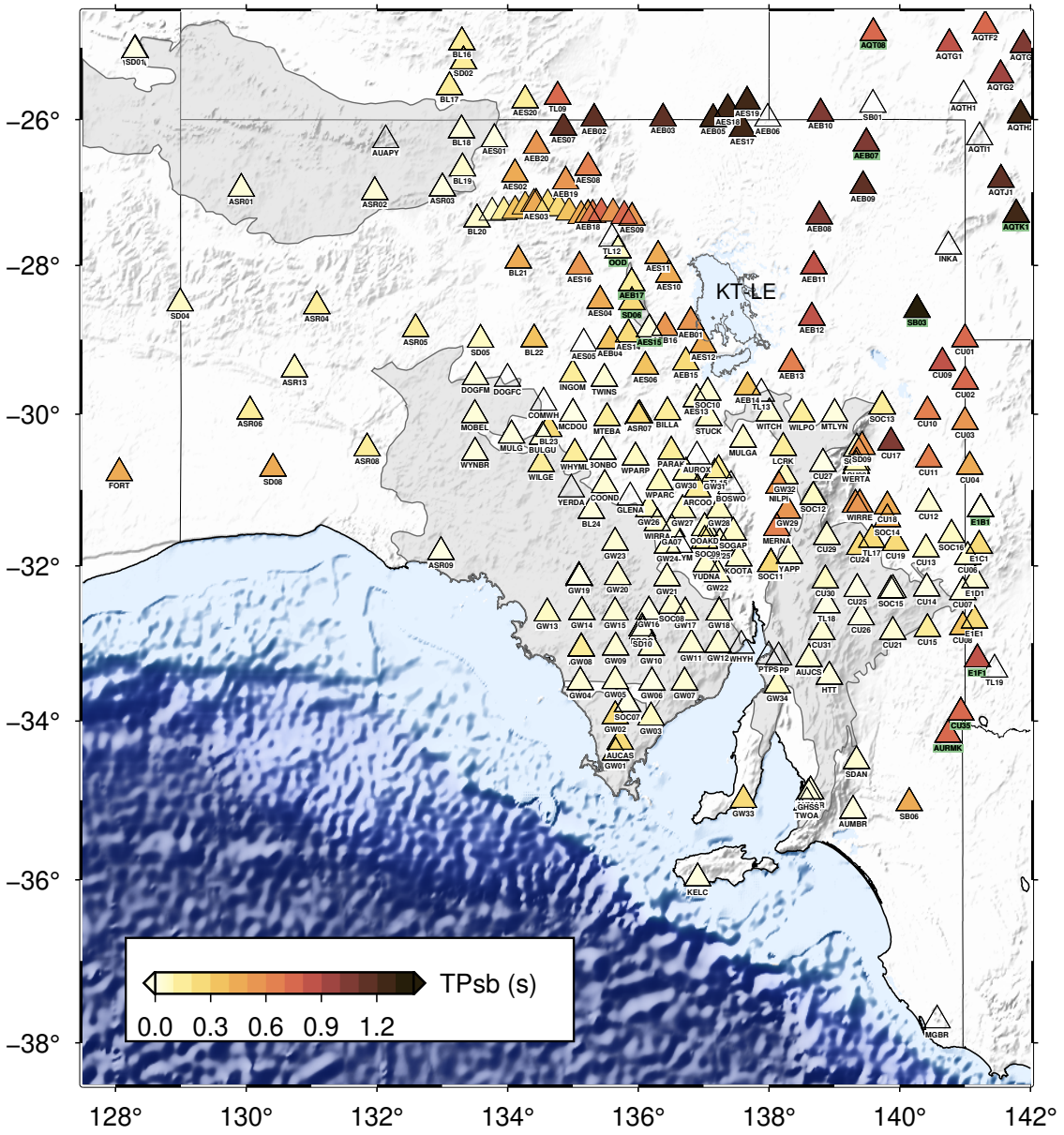

Figure 5. Values for times of arrivals of P-to-S converted phase (TPs_{b}) at the basement for seismic stations in South Australia. TPs_{b} values are estimated from receiver functions, as illustrated in Fig. 3. Transparent triangles are stations where receiver functions did not pass quality control. Stations names highlighted with green are stations discussed in the text. Gray shaded areas are the same as the dashed geological provinces in Fig. 2. KT-LE: Kati Thanda-Lake Eyre.

and Arckaringa Basins. The highest values of TPs_{b} ($\sim$1 s or more) are located in regions with several overlapping sedimentary sequences, such as in the northeast where the Lake Eyre, Eromanga, Cooper, and Warburton Basins overlap. Notably, for stations situated on top of the oldest basins such as Officer and Cariewerloo Basins, the TPs_{b} values are close to zero ($\leq$ 0.2 s). As noted from Table 1, the seismic velocities of these Proterozoic basins are often similar in value to the expected

basement velocity ($\sim$5 km/s or higher), reducing the impedance contrast, and thus making older Proterozoic sedimentary basins less sensitive to the RF technique. Nonetheless, it is evident from the above that the TPs_{b} variations capture both small-scale and large-scale sedimentary features across South Australia, and therefore can be utilized to estimate the depth to basement beneath each seismic station.

3.3 Calibration of TPs_{b} with borehole basement depth

An expansive dataset of borehole drill sites within South Australia (Fig. 2) offers a unique opportunity to compare and calibrate the relationship between TPs_{b} and the basement depth. Of the 243 seismic stations located in South Australia (Fig. 5), 85% are located within 0.5° of a borehole site. It is often the case, however, that the seismic stations are located near multiple boreholes; therefore, in order to directly compare, an average value of borehole basement depth must be calculated for each station. We chose to interpolate the borehole basement depth values surrounding each station using the inverse distance weighting (IDW) method (Shepard, 1968). This method assigns a single basement depth value based on a weighted average of the borehole values within 0.5° of a station. If no borehole measurement was found within 0.5° of a station, no basement depth was assigned to it. The weighting given to each borehole value is based on the inverse of the distance to the station to the power of *p*, chosen here as 2. This takes into account the relative proximity of borehole points to the stations, thus making sure the interpolated basement depth at a station is dominated by the values which are closest and is less likely to be skewed by a single aberrant value.

The IDW method returned an interpolated basement depth beneath 182 seismic stations, represented as circles in Fig. 6. We divide the stations in two categories based on the age of the sedimentary rock beneath the stations. Stations situated atop Phanerozoic sedimentary rocks are shown as turquoise coloured circles while stations on predominantly Proterozoic sedimentary rocks are pink. Although there is some scatter, an overall positive correlation between TPs_{b} and interpolated borehole basement depth can be recognized, with larger TPs_{b} arrival times corresponding to deeper borehole basement depths (Fig. 6). This positive trend is reinforced when the median

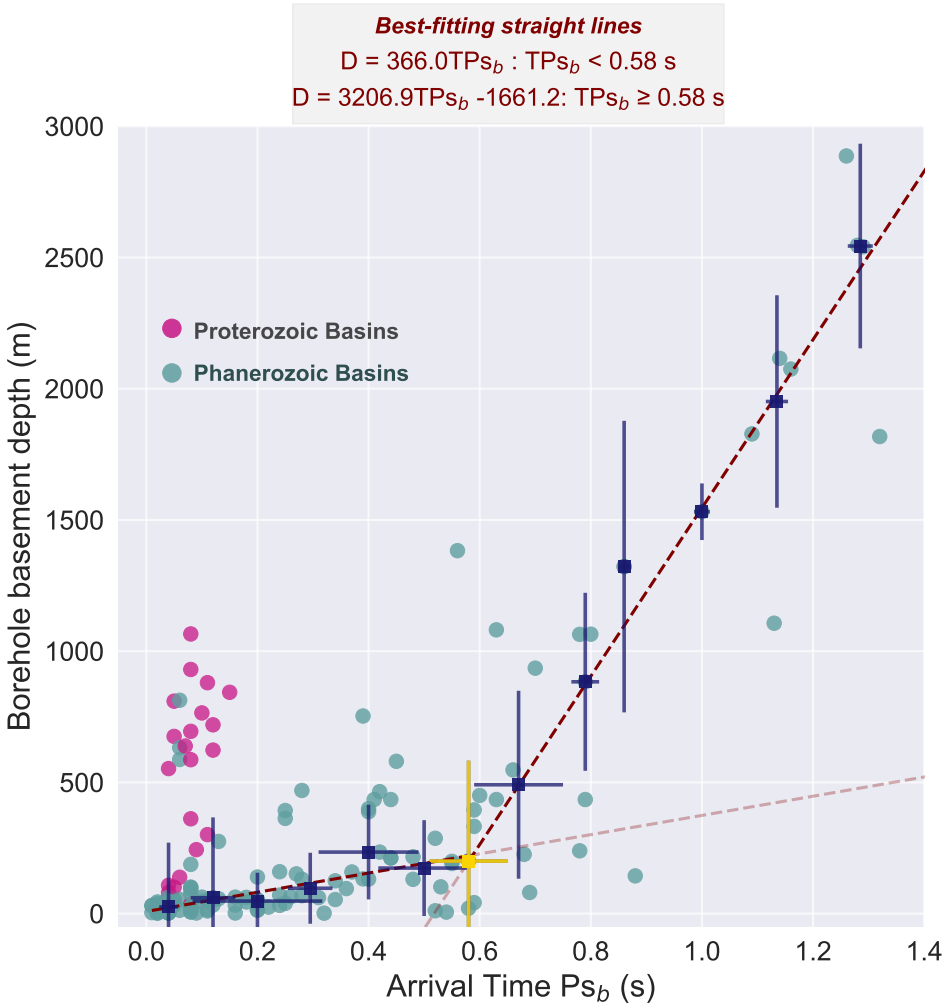

Figure 6. Statistical comparison of the receiver function estimated TPs_{b} and borehole basement depth beneath 182 seismic stations, plotted as circles. Turquoise circles are stations situated atop Phanerozoic Basins while pink are on Proterozoic Basins. Dark blue squares are the binned median values for every 0.09 s, with vertical solid blue lines representing the standard deviation. Horizontal blue lines are the errors in TPs_{b} measurements estimated by frequency analysis. The magnitude of these errors are calculated by averaging the absolute δTPs_{b} values for the 4 Hz frequency cut-off band (Fig. S4d). The yellow square denotes the point of inflection in the data, about which two linear equations (maroon dotted lines with equations at top) are regressed. RMSE: Root Mean Square Error.

values (with standard deviation) are plotted for each data bin (blue squares with vertical errorbars, Fig. 6). The gradient of the trend however is not constant, with basement depths gradually increasing for arrival times between 0 and ~0.6 seconds and more steeply increasing thereafter. A linear regression on the binned median values (blue squares), using standard deviations as the weights, is performed to fit two lines that share TPs_{b} = 0.58 s as a common point (yellow square). If a

different common point is chosen, then the residual error increases (Fig. S5). The fitted straight lines are of the form,

$$D = 366TPs_{\mathrm{b}}, \quad for \;\; TPs_{\mathrm{b}} < 0.58s \tag{1}$$

and

$$D = 3206.9TPs_{\mathrm{b}} - 1661.2, \quad for \;\; TPs_{\mathrm{b}} \geqq 0.58s, \tag{2}$$

where TPs_{b} is in seconds and D is the depth to basement in meters. It is to be noted, however that Equations 1 and 2 represent the best fitting linear trends, but the true relationship between the basement depth and TPs_{b} might not be linear. A best-fitting exponential and quadratic relationship was also explored (Fig. S6), but both of these yielded higher RMSE values than the linear equations. Further, the non-linear curves diverge rapidly for $TPs_{\mathrm{b}} > 1.5$ s. Additional data from deeper sedimentary basins (basement depth $>$ 4000 m) may help further constrain this in the future.

As noted in Fig. 3, for the case of vertically incident P and S waves beneath the station, basement depth and TPs_{b} are related as,

$$D = \frac{TPs_{\mathrm{b}} \times Vp_{\mathrm{sedi}} \times Vs_{\mathrm{sedi}}}{Vp_{\mathrm{sedi}} - Vs_{\mathrm{sedi}}}, \tag{3}$$

where $\mathrm{Vp_{sedi}}$ and $\mathrm{Vs_{sedi}}$ are the average seismic velocities across the total depth extent of the sedimentary basin. It is evident that calibrated Equations 1 and 2 are simplified forms of Equation 3 and that the gradient in Fig. 6 is a function of the seismic velocities of the sedimentary rock. As expected, deeper sedimentary basins ($>$ 500 m) display a steeper gradient indicating faster seismic velocities that likely result from increased compaction at depth.

To ascertain the reliability of TPs_{b} picks, we perform horizontal to vertical spectral ratio analysis (HVSR; e.g. Nakamura, 1989, 2019) for 38 stations of the Lake Eyre array. HVSR has been used widely to understand the Earth's shallow structure using both ambient noise and arrivals from earthquake records (e.g. Nishitsuji et al., 2014; Cipta et al., 2018; Schleicher & Pratt, 2021). We refer the reader to a recent review by Molnar et al. (2022) for a comprehensive understanding of

the topic. Here, we implement the methodology of Cox et al. (2020) to calculate the dominant resonance frequency (with uncertainties) of the sediment layer using seismic ambient noise (1-2 hr of seismically quiescent data). This analysis was performed individually for the stations using *hvsrpy* Python package (Vantassel, 2020, example shown in Fig. S7 for four stations with varying sediment thickness). The obtained fundamental frequencies beneath individual stations are juxtaposed with the TPs_{b} values and the borehole basement depth in Fig. S8. It is well established that the fundamental frequency of the sediment layer decreases with increasing sediment thickness (e.g. Field & Jacob, 1993; Ibs-von Seht & Wohlenberg, 1999); therefore, the fundamental frequency should also be inversely proportional to TPs_{b}, which is distinctly observed in Fig. S8. Further, a clear inverse relation is also noted between fundamental frequency and borehole basement depth. These two unmistakable trends, obtained using independent HVSR methodology, demonstrate the viability of our receiver function based method.

While the seismic velocities within sedimentary basins may vary in other settings, for our study region, the calibrated equations (1 and 2) seem to provide a reasonable fit to the available borehole data. We, therefore, use the calibrated equations to estimate the basement depth beneath all seismic stations in South Australia (Fig. 7), hereafter referred to as the RF basement depth.

3.4 Comparison of seismically determined basement depth with the pattern of sedimentation across South Australia (SA)

Using the calibrated equations the RF estimated depth to basement for all stations correlates strongly with the extent of and spatial trends in sedimentation for South Australia (Fig. 7), even taking into account the expected errors, i.e., $\pm$134 m for the shallower and $\pm$360 m for the deeper sedimentary basins (discussed in more detail in next section). In the northeastern part of the study region, the RF estimated depths are highest, with values between 1000-2800 m, due to the superposition of Cooper and Eromanga Basins. Outside the boundary of Cooper Basin (green coloured basin in Fig. 7b), the basement depth decreases as seen in the borehole values. AQT network stations in Queensland expand the basement depth knowledge in this region. Station AQTK1, which

is inside the Cooper basin, registers a depth of 2,352 m; in comparison, AQT08, located to the northwest outside of the Cooper Basin, records a shallower depth of 620 m, suggesting decreasing sedimentary rock thickness moving northwards. South of the Cooper Basin along the SA-NSW border, the basement depth gets progressively shallower (830 m at station CU01 to $\sim$10 m at station E1B1), representing the thinning Eromanga Basin until its southernmost extent near Cockburn (Fig. 1). South of Cockburn, the RF basement depth slightly increases again (100-300 m) due to the Cenozoic Murray Basin bounded to the west by the Flinders Ranges. Notably, three stations (E1F1, CU35, AURMK) close to the SA-NSW-Victoria border show significantly deeper values (600-900 m) due to the presence of the concealed Mesozoic Berri Basin. This adds further constraints to the boundary of Berri Basin, which is more sparsely sampled by borehole drilling (Fig. 7a).

Near the border between SA and the Northern Territory (26° S), there is a dramatic change in the RF basement depth around longitude 134° E. East of this location, within the Simpson Desert, the RF estimated depth to the Proterozoic crystalline basement ranges between 2200-2500 m due to the combined sedimentation from the Warburton, Pedrika, Eromanga, and Lake Eyre Basins. These stations in the Simpson Desert, which belong to the Lake Eyre Basin array, are the first to be deployed in the region, thus providing new basement depth constraints for hitherto underexplored parts of Australia. West of 134° E marks the low-sediment region of the exhumed Musgrave province, the result of the Petermann Orogeny around 570-530 Ma (e.g. Wade et al., 2008). Stations located within the Musgrave province record typically shallow RF basement depths of $<$ 25 m. The Marla Line experiment (3G), a dense east-west linear transect of seismic stations, further illustrates the decreasing sedimentary rock thickness from the east (750-1000m) to the west (10-100m) due to thinning of the Eromanga Basin. South of Oodnadatta, four stations (OOD, AEB17, SD06, AES15) show shallower basement depth ($<$ 70 m) compared to the surrounding stations (150-300 m). These stations sit on Neoproterozoic Denison and Peake Inliers surrounded by Eromanga Basin with Arckaringa Basin to the west.

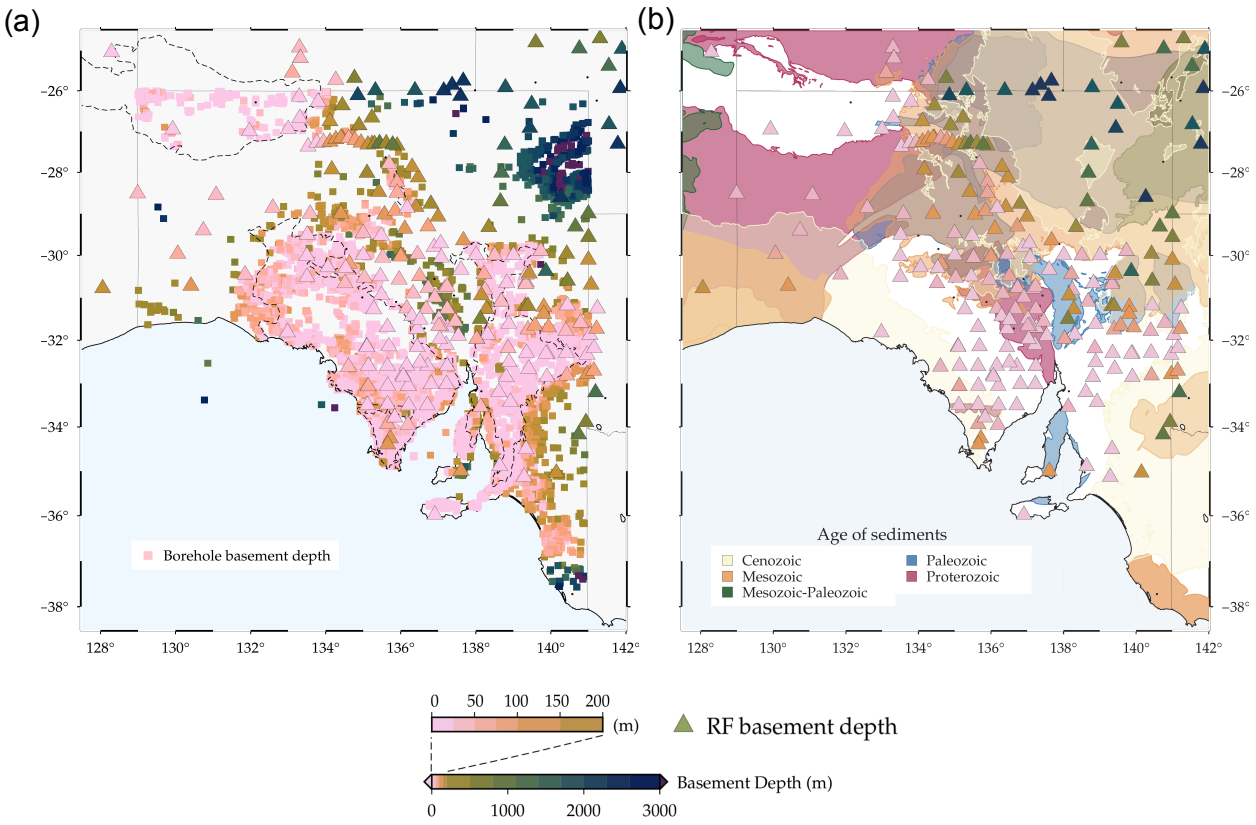

Figure 7. Receiver function estimated basement depth (coloured triangles) juxtaposed with (a) borehole measurements (same as Fig. 2) and (b) sedimentary basins (same as Fig. 1). The black dots are stations that didn't pass quality control. It is to be noted that in (b), the basins are coloured by the age of sediments, while the stations are coloured according to the RF basement depth, given by the legend below the figure.

The southern part of the Gawler Craton has areas of exposed Paleoproterozoic-Archean crust with little to no sediment cover, which is well represented by estimated basement depths of $<$ 50 m. However, for stations atop Proterozoic Basins like the Officer, Amadeus, and Cariewerloo Basins the RF basement depths do not match the borehole values (pink circles in Fig. 6). Within the boundaries of Mesoproterozoic Cariewerloo Basin, this is especially evident, with borehole basement depths of up to 1,500 m. Contrastingly, the RF estimated basement depth is $<$ 100 m. This can be explained as older Proterozoic sedimentary rocks are often heavily metamorphosed with increased seismic velocities and Vp values potentially greater than 5.8 km/s (Table 1; Wang et al., 2016), therefore inhibiting a strong impedance contrast with the crystalline basement. Given the propensity of base metals to be hosted in such Proterozoic basins (Hitzman et al., 2010; Leach et al., 2010), our method may be useful in determining the top of Proterozoic sedimentary rock

instead. These regions of older and seismically faster Proterozoic basins produce the anomalous cluster of data points in Fig. 6 (pink circles) with borehole depth values between 500-1000 m for $TPs_{\mathrm{b}} < 0.2$ s.

3.5 Uncertainties in RF basement depth estimation

The RF estimated basement depths appear to match the sedimentary basin and borehole values reasonably well. The typical error in basement depth for TPs_{b} measurements $\leq$0.6s is $\pm$134 m. This is estimated from the standard deviation within each data bin (i.e. the average length of the dark blue vertical errorbars in Fig. 6). The computed error for TPs_{b} $\leq$0.6s is further visualized in Fig. S9. For TPs_{b} measurements $\geq$0.6s, the typical error in the basement depth, or rather the amplitude of the error-bars in Fig. 6, increases to $\pm$360 m on average. As fewer deeper boreholes have been drilled (Fig. S2) there are fewer data points for TPs_{b} values $\geq$0.6s, which partially contributes to some of the increased uncertainty where there is a substantial difference between a small number of points within a given data bin (Fig. 6). Error in the estimated basement depth is expected due to several reasons. These are outlined further below.

Firstly, the calibrated relationship between Ps_{b} arrival time and the basement depth (Fig. 6) is based on the amalgamation across South Australia of available data-points (either seismic RF or borehole basement depths). For a given seismic station, it is assumed that information from the nearby (within 0.5°) borehole sites also reflect the physical properties directly beneath the seismic station. Where the borehole distribution is relatively sparse however it is possible that the basement depth may vary between the seismic station and the closest available boreholes.

Secondly, the Ps_{b} phase arrival time is a function of both the sedimentary thickness, and the difference between the average P-wave versus S-wave slowness through the sedimentary basin (equation 3). We are therefore assuming that this difference in slowness is similar for different sedimentary basins, or rather that the seismic velocities increase with depth in a similar manner within all the sedimentary basins across South Australia. However, as Table 1 suggests, this may

not always be the case, particularly if the lithology of the sedimentary rocks changes substantially between different basins. This likely accounts for a large extent of the range of scatter seen in Fig. 6.

Thirdly, one of our primary assumptions is that in the presence of sediments, there is insignificant P-wave energy on the horizontal components; thus, the highest amplitude on the radial RF is due to the Ps_b phase. However, as discussed previously, in regions of thin or well-compacted sediments, this might not always be the case, and there could be a potential overlap of direct P and Ps_b phase or PPs_b and Ps_b phase, which may slightly underestimate or overestimate the RF derived basement depth. The magnitude of this error is expected to be $\pm$ 0.125 seconds as revealed by RF analysis at different frequencies (Fig. S4). Further, in the presence of horizontal scatters (for example, basin edges), the Ps_b phase arrival could differ according to the earthquake backazimuth (e.g. Fig. S10, for station AEB04). If significant scattering effects are observed in the individual RFs, then it is crucial to have a good backazimuthal earthquake coverage so that the Ps_b phase in the stack is not influenced by limited backazimuths.

Fourthly, it is assumed the largest impedance contrast, representing the first and largest amplitude peak in the RF, is generated by the boundary between the crustal basement and the overlying sedimentary rock. As has been identified, this assumption appears to hold true for Phanerozoic sedimentary basins but fails for the oldest Proterozoic basins. Older sedimentary rocks are more likely to be metamorphosed, resulting in higher seismic velocities, with less distinction between 'sediments' and the underlying basement (Table 1). In such cases, the TPs_b values can appear anomalously low ($<$ 0.2 s), which may be misinterpreted as a thin layer of sediments ($<$ 200 m) if the geological context is not considered or is unknown.

Lastly, when applying the obtained empirical equations for basement depth (equations 1 & 2), some important considerations need to be kept in mind. Firstly, the associated errors could potentially be too large for some applications where tight constraints are needed, such as oil and

gas exploration, and therefore caution is advised as the obtained basement depth should be treated as an initial estimate. Secondly, for stations located on thin sediments (i.e. thickness $\leq$ 500m), the authors encourage to compare results by including higher frequency bands and checking if the picked pulse is unequivocally the Ps_b phase. Thirdly, the obtained basement depths should ideally be juxtaposed with regional geological knowledge. This is important as the RF are sensitive to the largest velocity difference in the sedimentary layers, and might not always reflect the total sedimentary rock thickness if the sediment velocities are comparable to the basement, or if the sediment velocities substantially differ from that of the regional average.

4 CONCLUSION AND FUTURE IMPLICATIONS

We present a novel yet simple method to estimate the depth to basement in the presence of varying sedimentary rock thickness using receiver functions. Using the borehole database of South Australia, we calibrate a relationship between the relative arrival time of the P-converted-to-S phase generated at the base of the sedimentary basin and the basement depth. The method was demonstrated using data from seismic stations across South Australia and is able to capture the known variations in Phanerozoic sedimentary rocks across the region, without a priori knowledge of the sub-surface velocity structure. We employed the method to provide depth to basement estimates at remote locations in South Australia beyond the geographic reach of the drillhole database, particularly in areas of deep sedimentary rocks such as the Simpson, Strzelecki, and Sturt Stony Deserts.

Despite the uncertainties, the methodology showcased here has three main advantages. Firstly, the calibrated equations can be employed to get a quick and credible assessment of total Phanerozoic sediment thickness using only temporary seismic stations deployed for less than 6 months, with little or no knowledge of the sub-surface velocity structure. Thus, it could serve as a pre-drill strategy to estimate the basement depth before physically deploying drilling equipment. This is particularly beneficial for deep basins, where drilling becomes increasingly expensive for deeper boreholes. Secondly, using temporary seismic stations for a few months is relatively inexpensive, and the acquired passive-seismic data will additionally be useful for many other applications to

image the Earth's interior. Thirdly, while our method can't determine the base of older Proterozoic basins, it may help determine the top of such metamorphosed sedimentary rocks, which is desirable for future sedimentary rock hosted base metal exploration projects, especially in places like Australia. Therefore, this method has immense potential for under-explored regions around the globe where rich mineral resources may currently be hidden under cover.

ACKNOWLEDGMENTS

We acknowledge the traditional custodians of South Australia on whose land the seismic stations were deployed. SA and CE are supported by Australian Research Council Grant DE190100062. We are grateful to the Editor Victor Cruz-Atienza, and the reviewers Justin Ball and Patricia Persaud for their helpful suggestions. We thank Vedran Lekic, Thomas Brocher, Anthony Reid, and Brian Kennett for providing comments on an earlier draft of this manuscript. The Lake Eyre Basin seismic array and many other previous temporary deployments were made possible via funding from AuScope (auscope.org.au), instrumentation from the Australian National Seismic Imaging Resource (ANSIR), and contributions from staff, especially Robert Pickle and Michelle Salmon, at the Research School of Earth Sciences, Australian National University. The AusArray SA deployment is supported by the Geological Survey of South Australia, with instrumentation from ANSIR and Geoscience Australia. SA thanks Matthias Scheiter for fruitful discussions and honest feedbacks. The GSSA thanks Bruce Goleby, Ann Goleby, Isaac Axford, Kate Selway, John Stephenson, Alexei Gorbatov, and Colin Telfer for their contribution to AusArray SA. We are incredibly grateful to landholders, traditional owners, and the Department of Defence for granting land access for the seismic arrays. JPOD publishes with the permission of the Director of the Geological Survey of South Australia.

DATA AVAILABILITY

The earthquakes used in this study were collected from Incorporated Research Institutions for Seismology (IRIS) Data Services (http://ds.iris.edu/ds/). The seismic waveform data from 14 seismic networks was used: 5G (doi:10.7914/SN/5G_2018); 6K (doi:10.7914/SN/6K_2020); 5J (http://www.fdsn.org/ne

7B (doi:10.7914/SN/7B_1993); 1F (doi:10.7914/SN/1F_2009); 6F (doi:10.7914/SN/6F_2008); YJ (http://www.fdsn.org/networks/detail/YJ_2009/); 7K (doi:10.7914/SN/7K_2007); 7I (doi:10.7914/SN/7I_2003) 1G (doi:10.7914/SN/1G_2008); 1Q (doi:10.7914/SN/1Q_2016); 3G (doi:10.7914/SN/3G_2018); S1 (doi:10.7914/SN/S1); AU (https://www.fdsn.org/networks/detail/AU/). The Python package 'rf' version 1.0.0 (Eulenfeld, 2020) was used to compute the receiver functions. All the seismic data was handled using the Python package Obspy (https://docs.obspy.org/; Krischer et al., 2015). HVSR analysis was done using the hvsrpy Python package (Vantassel, 2020). Borehole data used in the study was obtained from the South Australian Resources Information Gateway and is titled 'Crystalline basement intersecting drillholes'(https://map.sarig.sa.gov.au/). Information about the active/operating mines in South Australia was obtained from the Department of Energy and Mining, Government of South Australia (https://energymining.sa.gov.au/). Plots were made using the Generic Mapping Tools, Version 6.1.1 (https://www.generic-mapping-tools.org/; Wessel et al., 2019) and Matplotlib version 3.4.2 (https://matplotlib.org/).

References

Ali, S. H., Giurco, D., Arndt, N., Nickless, E., Brown, G., Demetriades, A., Durrheim, R., Enriquez, M. A., Kinnaird, J., Littleboy, A., et al., 2017. Mineral supply for sustainable development requires resource governance, *Nature*, **543**(7645), 367–372.

Allen, T. I., Griffin, J. D., Leonard, M., Clark, D. J., & Ghasemi, H., 2020. The 2018 national seismic hazard assessment of australia: Quantifying hazard changes and model uncertainties, *Earthquake Spectra*, **36**(1_suppl), 5–43.

Ammon, C. J., 1991. The isolation of receiver effects from teleseismic p waveforms, *Bulletin of the seismological Society of America*, **81**(6), 2504–2510.

Baines, G., Giles, D., & Betts, P., 2010. 3d geophysical modelling of the northern gawler craton, south australia, *Geoscience Australia, Record*, **39**, 95–107.

Barham, M., Reynolds, S., Kirkland, C., O'Leary, M., Evans, N., Allen, H., Haines, P., Hocking, R., & McDonald, B., 2018. Sediment routing and basin evolution in proterozoic to mesozoic east gondwana: A case study from southern australia, *Gondwana Research*, **58**, 122–140.

Birkey, A., Ford, H. A., Dabney, P., & Goldhagen, G., 2021. The lithospheric architecture of australia from seismic receiver functions, *Journal of Geophysical Research: Solid Earth*, **126**(4), e2020JB020999.

Bishop, C., 2012. Interpretation and modelling of the pedirka basin (central australia) using magnetics, gravity, well-log and seismic data, *ASEG Extended Abstracts*, **2012**(1), 1–4.

Brocher, T. M., 2005. Empirical relations between elastic wavespeeds and density in the earth's crust, *Bulletin of the seismological Society of America*, **95**(6), 2081–2092.

Brown, C. M. & Stephenson, A. E., 1991. Geology of the murray basin, southeastern australia, *Bulletin-Australia, Bureau of Mineral Resources, Geology and Geophysics*, (235).

Cassidy, J., 1992. Numerical experiments in broadband receiver function analysis, *Bulletin of the Seismological Society of America*, **82**(3), 1453–1474.

Cipta, A., Cummins, P., Dettmer, J., Saygin, E., Irsyam, M., Rudyanto, A., & Murjaya, J., 2018. Seismic velocity structure of the jakarta basin, indonesia, using trans-dimensional bayesian inversion of horizontal-to-vertical spectral ratios, *Geophysical Journal International*, **215**(1),

431–449.

Collett, D. & McFadden, P., 2014. Uncover initiative: ushering in a new era of exploration in australia.

Cox, B. R., Cheng, T., Vantassel, J. P., & Manuel, L., 2020. A statistical representation and frequency-domain window-rejection algorithm for single-station hvsr measurements, *Geophysical Journal International*, **221**(3), 2170–2183.

Cunningham, E. & Lekic, V., 2019. Constraining crustal structure in the presence of sediment: a multiple converted wave approach, *Geophysical Journal International*, **219**(1), 313–327.

Cunningham, E. & Lekic, V., 2020. Constraining properties of sedimentary strata using receiver functions: An example from the atlantic coastal plain of the southeastern united states, *Bulletin of the Seismological Society of America*, **110**(2), 519–533.

Drexel, J. & Preiss, W., 1995. The geology of south australia, vol. 2. the phanerozoic: South australia geological survey, *Bulletin*, **55**.

Eakin, C., 2019. Seismicity, minerals, and craton margins: The lake eyre basin seismic deployment, *ASEG Extended Abstracts*, **2019**(1), 1–2.

Eulenfeld, T., 2020. rf: Receiver function calculation in seismology, *Journal of Open Source Software*, **5**(48), 1808.

Field, E. & Jacob, K., 1993. The theoretical response of sedimentary layers to ambient seismic noise, *Geophysical research letters*, **20**(24), 2925–2928.

Fraser, G., Blewett, R., Reid, A., Korsch, R., Dutch, R., Neumann, N., Meixner, A., Skirrow, R., Cowley, W., Szpunar, M., et al., 2010. Geological interpretation of deep seismic reflection and magnetotelluric line 08ga-g1: Eyre peninsula, gawler craton, south australia, in *South Australian seismic and MT workshop*, vol. 10, pp. 81–95.

Hand, M., Reid, A., & Jagodzinski, L., 2007. Tectonic framework and evolution of the gawler craton, southern australia, *Economic Geology*, **102**(8), 1377–1395.

Hitzman, M. W., Selley, D., & Bull, S., 2010. Formation of sedimentary rock-hosted stratiform copper deposits through earth history, *Economic Geology*, **105**(3), 627–639.

Hoggard, M. J., Czarnota, K., Richards, F. D., Huston, D. L., Jaques, A. L., & Ghelichkhan, S.,

2020. Global distribution of sediment-hosted metals controlled by craton edge stability, *Nature Geoscience*, **13**(7), 504–510.

Ibs-von Seht, M. & Wohlenberg, J., 1999. Microtremor measurements used to map thickness of soft sediments, *Bulletin of the Seismological Society of America*, **89**(1), 250–259.

Kennett, B. & Engdahl, E., 1991. Traveltimes for global earthquake location and phase identification, *Geophysical Journal International*, **105**(2), 429–465.

Kennett, B., Salmon, M., Saygin, E., & Group, A. W., 2011. Ausmoho: the variation of moho depth in australia, *Geophysical Journal International*, **187**(2), 946–958.

Korsch, R., Blewett, R., Giles, D., Reid, A., Neumann, N., Fraser, G., Holzshuh, J., Costelloe, R., Roy, I., Kennett, B., et al., 2010. Geological interpretation of the deep seismic reflection and magnetotelluric line 08ga-om1: Gawler craton-officer basin-musgrave province-amadeus basin (goma), south australia and northern territory, in *GOMA (Gawler Craton-Officer Basin-Musgrave Province-Amadeus Basin) Seismic and MT Workshop*, pp. 63–86.

Krischer, L., Megies, T., Barsch, R., Beyreuther, M., Lecocq, T., Caudron, C., & Wassermann, J., 2015. Obspy: A bridge for seismology into the scientific python ecosystem, *Computational Science & Discovery*, **8**(1), 014003.

Langston, C. A., 1979. Structure under mount rainier, washington, inferred from teleseismic body waves, *Journal of Geophysical Research: Solid Earth*, **84**(B9), 4749–4762.

Leach, D. L., Bradley, D. C., Huston, D., Pisarevsky, S. A., Taylor, R. D., & Gardoll, S. J., 2010. Sediment-hosted lead-zinc deposits in earth history, *Economic Geology*, **105**(3), 593–625.

Li, G., Yang, Y., Niu, F., & Chen, M., 2021. 3-d sedimentary structures beneath southeastern australia constrained by passive seismic array data, *Journal of Geophysical Research: Solid Earth*, **126**(2), e2020JB019998.

Liang, S. & Kennett, B. L., 2020. Passive seismic imaging of a craton edge–central australia, *Tectonophysics*, **797**, 228662.

Ligorría, J. P. & Ammon, C. J., 1999. Iterative deconvolution and receiver-function estimation, *Bulletin of the seismological Society of America*, **89**(5), 1395–1400.

Liu, G., Persaud, P., & Clayton, R. W., 2018. Structure of the northern los angeles basins revealed

in teleseismic receiver functions from short-term nodal seismic arrays, *Seismological Research Letters*, **89**(5), 1680–1689.

Molnar, S., Sirohey, A., Assaf, J., Bard, P.-Y., Castellaro, S., Cornou, C., Cox, B., Guillier, B., Hassani, B., Kawase, H., et al., 2022. A review of the microtremor horizontal-to-vertical spectral ratio (mhvsr) method, *Journal of Seismology*, pp. 1–33.

Mudd, G., Czarnota, K., Skirrow, R. G., McAlpine, S., Yuan, Y., Yellishetty, M., Weng, Z.-H., & Werner, T., 2019. *Critical Minerals in Australia: A review of opportunities and research needs*, Geoscience Australia.

Mudd, G. M., 2007. *The sustainability of mining in Australia: key production trends and their environmental implications for the future*, Department of Civil Engineering, Monash University.

Nakamura, Y., 1989. A method for dynamic characteristics estimation of subsurface using microtremor on the ground surface, *Railway Technical Research Institute, Quarterly Reports*, **30**(1).

Nakamura, Y., 2019. What is the nakamura method?, *Seismological Research Letters*, **90**(4), 1437–1443.

Nishitsuji, Y., Ruigrok, E., Gomez, M., & Draganov, D., 2014. Global-phase h/v spectral ratio for delineating the basin in the malargüe region, argentina, *Seismological Research Letters*, **85**(5), 1004–1011.

Okada, H., 2006. Theory of efficient array observations of microtremors with special reference to the spac method, *Exploration Geophysics*, **37**(1), 73–85.

ODonnell, J., Thiel, S., Robertson, K., Gorbatov, A., & Eakin, C., 2020. Using seismic tomography to inform mineral exploration in south australia: The ausarray sa broadband seismic array, *MESA Journal*, **93**, 24–31.

Pain, C. F., Pillans, B. J., Roach, I. C., Worrall, L., & Wilford, J. R., 2012. Old, flat and red–australias distinctive landscape, *Shaping a nation: A geology of Australia*, pp. 227–275.

Piana Agostinetti, N., Martini, F., & Mongan, J., 2018. Sedimentary basin investigation using receiver function: an east african rift case study, *Geophysical Journal International*, **215**(3), 2105–2113.

Radke, B., 2009. *Hydrocarbon and geothermal prospectivity of sedimentary basins in central Australia: Warburton, Cooper, Pedirka, Galilee, Simpson and Eromanga basins*, Geoscience Australia.

Rawlinson, N., Stephenson, R., & Carbonell, R., 2017. Seismic imaging at the cross-roads: Active, passive, exploration and solid earth, *Tectonophysics*, **718**, 1–8, Seismix 2016: Advances in active and passive seismic imaging of continents and their margins.

Raymond, O., Totterdell, J., Woods, M., & AJ, S., 2018. Australian geological provinces 2018.01 edition, *Geoscience Australia, Canberra*.

Reid, A., 2019. The olympic cu-au province, gawler craton: a review of the lithospheric architecture, geodynamic setting, alteration systems, cover successions and prospectivity, *Minerals*, **9**(6), 371.

Schleicher, L. S. & Pratt, T. L., 2021. Characterizing fundamental resonance peaks on flat-lying sediments using multiple spectral ratio methods: An example from the atlantic coastal plain, eastern united states, *Bulletin of the Seismological Society of America*, **111**(4), 1824–1848.

Sheehan, A. F., Abers, G. A., Jones, C. H., & Lerner-Lam, A. L., 1995. Crustal thickness variations across the colorado rocky mountains from teleseismic receiver functions, *Journal of Geophysical Research: Solid Earth*, **100**(B10), 20391–20404.

Shepard, D., 1968. A two-dimensional interpolation function for irregularly-spaced data, in *Proceedings of the 1968 23rd ACM national conference*, pp. 517–524.

Southgate, P., Neumann, N., & Gibson, G., 2013. Depositional systems in the mt isa inlier from 1800 ma to 1640 ma: Implications for zn–pb–ag mineralisation, *Australian Journal of Earth Sciences*, **60**(2), 157–173.

Srinivas, D., Srinagesh, D., Chadha, R., & Ravi Kumar, M., 2013. Sedimentary thickness variations in the indo-gangetic foredeep from inversion of receiver functions, *Bulletin of the Seismological Society of America*, **103**(4), 2257–2265.

Tao, K., Liu, T., Ning, J., & Niu, F., 2014. Estimating sedimentary and crustal structure using wavefield continuation: theory, techniques and applications, *Geophysical Journal International*, **197**(1), 443–457.

Tauzin, B., van der Hilst, R. D., Wittlinger, G., & Ricard, Y., 2013. Multiple transition zone seismic discontinuities and low velocity layers below western united states, *Journal of Geophysical Research: Solid Earth*, **118**(5), 2307–2322.

Vantassel, J., 2020. jpvantassel/hvsrpy: v0. 2.1 (version v0. 2.1). zenodo.

Vinnik, L., 1977. Detection of waves converted from p to sv in the mantle, *Physics of the Earth and planetary interiors*, **15**(1), 39–45.

Wade, B., Kelsey, D., Hand, M., & Barovich, K., 2008. The musgrave province: stitching north, west and south australia, *Precambrian Research*, **166**(1-4), 370–386.

Wang, M., Hubbard, J., Plesch, A., Shaw, J. H., & Wang, L., 2016. Three-dimensional seismic velocity structure in the sichuan basin, china, *Journal of Geophysical Research: Solid Earth*, **121**(2), 1007–1022.

Wang, X., Zhan, Z., Zhong, M., Persaud, P., & Clayton, R. W., 2021. Urban basin structure imaging based on dense arrays and bayesian array-based coherent receiver functions, *Journal of Geophysical Research: Solid Earth*, **126**(9), e2021JB022279.

Wessel, P., Luis, J., Uieda, L., Scharroo, R., Wobbe, F., Smith, W., & Tian, D., 2019. The generic mapping tools version 6, *Geochemistry, Geophysics, Geosystems*, **20**(11), 5556–5564.

Yeates, A., Gibson, D., Towner, R., & Crowe, R., 1984. Regional geology of the onshore canning basin, wa.

Yeck, W. L., Sheehan, A. F., & Schulte-Pelkum, V., 2013. Sequential h-κ stacking to obtain accurate crustal thicknesses beneath sedimentary basins, *Bulletin of the Seismological Society of America*, **103**(3), 2142–2150.

Yu, Y., Song, J., Liu, K. H., & Gao, S. S., 2015. Determining crustal structure beneath seismic stations overlying a low-velocity sedimentary layer using receiver functions, *Journal of Geophysical Research: Solid Earth*, **120**(5), 3208–3218.

Zang, W.-L., Jago, J., Alexander, E., & Paraschivoiu, E., 2004. A review of basin evolution, sequence analysis and petroleum potential of the frontier arrowie basin, south australia.

Zelt, B. & Ellis, R., 1999. Receiver-function studies in the trans-hudson orogen, saskatchewan, *Canadian Journal of Earth Sciences*, **36**(4), 585–603.

Zhang, Z. & Olugboji, T., 2021. The signature and elimination of sediment reverberations on submarine receiver functions, *Journal of Geophysical Research: Solid Earth*, **126**(5), e2020JB021567.

Zheng, T., Zhao, L., & Chen, L., 2005. A detailed receiver function image of the sedimentary structure in the bohai bay basin, *Physics of the Earth and Planetary Interiors*, **152**(3), 129–143.